Merle Richter*, Yannik Loth, Christian Weisenstein, Anna Katharina Wigger, Dominik Schaar, Anja Katrin Bosserhoff and Peter Haring Bolívar

Ultrasensitive marker-free biomolecular THz-detection for tumor-related analytics

https://doi.org/10.1515/freq-2022-0092
Received April 26, 2022; accepted June 30, 2022;
published online August 5, 2022

Abstract: Terahertz (THz) biosensing has emerged as an important research field, mainly driven by the resonant behavior of many biomolecules in this spectral range which holds potential for highly sensitive analyses. In this work, we present a detailed overview of our current research on THz biosensing, focusing on the development and analysis of THz biosensors based on frequency selective surfaces (FSS) for two different measurement scenarios: i) label-free, highly sensitive and selective analysis of dried biomolecules, and ii) sensitive and selective analysis in an aqueous environment. With our carefully designed THz biosensor for measurements in the dry state, we were able to indirectly measure tumor-marker MIA RNA in a concentration as low as 1.55×10^{-12} mol/L, without the need for biochemical amplification. Our biosensor with substrate-integrated microfluidics for terahertz measurements in an aqueous environment is validated by simulations, showing that the resonance feature in the frequency response of our sensor is maintained even for measurements in water.

Keywords: biomedical spectroscopy; biosensing; fano resonance; metamaterial; microfluidics; terahertz.

***Corresponding author: Merle Richter**, University of Siegen, Institute for High Frequencies and Quantum Electronics, Siegen, Germany, E-mail: merle.richter@uni-siegen.de. https://orcid.org/0000-0002-8597-3877

Yannik Loth, Christian Weisenstein, Anna Katharina Wigger and Peter Haring Bolívar, University of Siegen, Institute for High Frequencies and Quantum Electronics, Siegen, Germany. https://orcid.org/0000-0003-4995-3200 (C. Weisenstein). https://orcid.org/0000-0001-5875-556X (P. Haring Bolívar)

Dominik Schaar and Anja Katrin Bosserhoff, Friedrich-Alexander-University, Institute for Biochemistry and Molecular Medicine, Erlangen, Germany, E-mail: anja.bosserhoff@fau.de (A.K. Bosserhoff)

1 Introduction

Despite the comparatively "young age" of significant THz research, THz radiation has attracted interest in a plethora of research areas due to its unique combination of properties and continues to be a rapidly growing research community. THz technology has become very important in various areas of research as well as industry [1–5] and partially already entered commercial applications. The THz frequency range is located at the long-wavelength end of the far-infrared electromagnetic spectrum and reaches up to the microwave regime. Especially intriguing for many non-invasive applications is therefore, that THz waves combine non-ionizing low energy radiation with high penetration depth for many materials [6–8]. Since most biomolecules and biomacromolecules exhibit resonant behavior in the THz spectrum, a large portion of its research is devoted to discover functional life science applications. Accordingly, one major aim is improving existing and developing entirely novel analytical tools in biomedical science for purposes including but not limited to disease diagnostics [9–11]. Among the different life sciences there is an interdisciplinary pursuit of achieving a qualitative description of an analyte as well as a quantitative assessment of its presence in a sample. In the process of moving beyond simply "observing" correlations towards "understanding" mechanisms in their complex network of interactions [12], a precise and reliable measurement result becomes more valuable but also much more difficult to achieve, the closer the sample matrix stays to the native environment it was taken from. Especially in the case of functional units like proteins whose interactions mainly depend on their three-dimensional shape, a large fraction of the potentially available information is easily lost when an analyte is isolated from its physiological environment. Direct investigation of more complex media also significantly simplifies sample preparation, thereby reducing the investment of personal resources, laboratory consumable supplies and ultimately cost. Consequently, one major goal of researchers in life sciences is to be able to detect and characterize a desired biomolecule in its diverse and reciprocal interaction-based native medium [13–15]. One important step in this direction is the real-time

measurement of bioanalytes in aqueous solutions which is particularly challenging for THz spectroscopy due to the high absorptive properties of water-based matrices.

As can be seen in Figure 1, the lower detection limit (LDL), or at least the lowest concentration in aqueous solutions that has been reported to be detected for standard analytical techniques seems to be several orders of magnitude lower in all analyte classes than could be obtained with THz methods so far. Since the term "biomolecule" covers an extremely large and diverse range of molecules, we introduce six categories differentiated by molecular weight, but also by function or chemical composition. Sodium cations (Na^+) represent the ionic analyte class [16–20], while carbohydrates are represented by glucose [21–23]. The group of nucleic acids of low to medium molecular weight is represented by the very similar molecules deoxyadenosine monophosphate (dAMP) and cyclic adenosine monophosphate (cAMP) [23–25]. Oxiplatin detection is displayed representatively for the active ingredients in medical drugs [26, 27]. Smaller proteins are represented by serum albumin (SA), more specifically bovine serum albumin (BSA) and human serum albumin (HSA) [23, 28, 29] whereas the heaviest biomacromolecules are represented by immunoglubolin G (igG) [30–32]. A more detailed analysis and overview

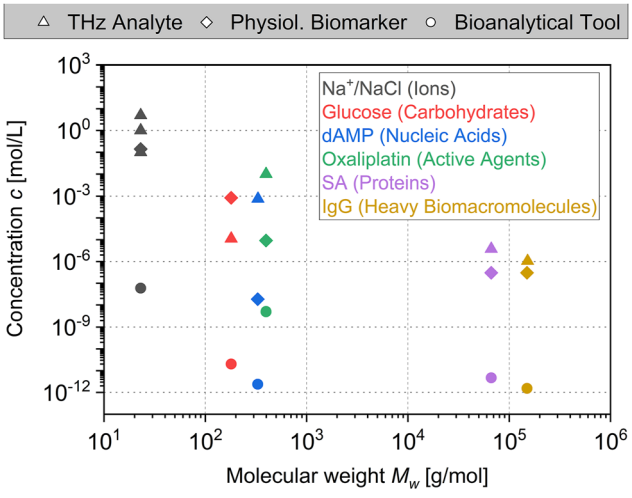

Figure 1: Diagram of the reported sensitivities (LDL values or lowest concentration detected) of physiologically relevant analytes measured using traditional THz sensing techniques (triangles) in aqueous solutions. Each analyte represents a class of bioanalytes. Different concentration levels of the same analyte refer to different reported values from different research groups (e.g. NaCl). The physiological concentration levels that symbolize a threshold sensitivity are marked as diamonds. Typical detection limits for state-of-the-art bioanalytical sensing techniques are displayed as circles for comparison [5].

of recent THz measurements of various interesting biomolecules and biomacromolecules in aqueous environments can be found in our review paper [33]. In order to establish THz analytical techniques among the life science standard analytical tools, this needs further research and enhancement of existing or development of entirely new methods. As a threshold concentration that should be detectable by techniques considered to be relevant, the physiological concentration of the corresponding analyte is marked as diamonds in Figure 1. At this point, it should be noted that Figure 1 does not provide information about the corresponding technique's performance and selectivity. Both can vary greatly depending on the method in question and play an important role when it comes to determining the significance of an analytical technique. One challenge for THz detection of biomedically interesting molecules is the large difference in size regarding the radiation wavelength (1 THz translates to approximately 300 µm) and the analyte dimensions (typically < 300 nm). For a significant interaction between radiation and matter to appear, highly concentrated samples are necessary, making analysis of physiological samples impossible. To overcome this obstacle, frequency selective surfaces (FSS), often referred to as metamaterials, are introduced as biosensor technology, being particularly sensitive to minute changes of the dielectric properties of a sample. FSS are arrays of resonators that exhibit a defined and, in the ideal case, sharp resonance feature in their frequency response. By application of a dielectric load to the FSS, the resonance frequency is detuned and the resonance feature is shifted in frequency. This frequency shift Δf can be determined sensitively using a THz spectroscopy system with appropriately high frequency resolution (in the order of 10 MHz for DNA detection). To achieve not only a very sensitive analysis, but also selectively provide information about the presence of a specific desired analyte, it is necessary to biochemically modify the sensor surface beforehand, e.g. by immobilizing a specific capture molecule to the sensor surface, which selectively binds to the target biomolecule.

Still, current THz metamaterial approaches mainly rely on the sample being dried before measurement, due to the very strong THz absorption of bulk water [34], which destroys the metamaterial resonance. However, since particularly the analysis of biomolecular interactions, binding and absorption processes, as well as the analysis of more complex biological systems is impossible in dry state, there have been recent attempts to realize metamaterial-based sensors that can also operate in water [35, 36]. For the water film thicknesses used there, i.e. 15–50 µm, which corresponds to the typical range of

microfluidic structures, the Q-factor and peak-to-peak transmission difference of the resonance feature is significantly reduced [29, 37–39] or disappears completely [40]. By applying metamaterials in a reflection setup [41] or reducing the water film thickness to 50 nm [42] or 160 nm [43], one can preserve the resonance feature at the cost of limited functionality or an increase in complexity of fabrication, structure or setup.

In this work, we present an overview of our recent THz biosensor research, beginning with THz biosensor development for DNA detection, including the biochemical sensor modification and THz analyses of tumor markers, followed by its further evolution towards the analysis of more complex biological systems in an aqueous environment. A particularly noteworthy result is the label-free THz detection of a tumor-marking mRNA sequence called melanoma inhibitory activity (MIA) in concentrations as low as 1.55×10^{-12} mol/L thereby superseding the need for biochemical amplification and labeling during sample preparation. These measurements are but one step on the path towards catching up with established bioanalytical techniques. This exceptionally high sensitivity is based on a carefully optimized sensor design, featuring an enhanced electric field concentration combined with localized selective biochemical sensor modification to refine the sensitivity and at the same time reduce the necessary sample volume. Based on this biosensor, we propose novel designs for sensor-integrated microfluidics in order to be able to measure also more complex biological systems in their natural environment. Our simulations show, that the resonance feature of our sensor designs is maintained even when measuring in aqueous solutions.

2 Methods

2.1 Specifications and devices

2.1.1 Simulation specifications: The modeling and simulation was performed with the 3D electromagnetic simulation software Ansys HFSS Electronics Desktop 2021R1. The unit cells were simulated as repetitive elements with the periodicity p, periodic boundary conditions and Floquet port excitation. The material parameters were constituted as follows: The dielectric constant for fused silica or quartz glass in the substrate and in the optional cover amounts to $\varepsilon_{r,q} = 3.81$ with a dielectric loss tangent $\delta_q = 0.0001$ [44, 45]. Its refractive index is approximately $n_q = 1.96$ and remains constant in the relevant frequency range [44]. The parameters for gold (Au) were extracted from the complex dielectric function of the Drude model: $\varepsilon_{r,Au} = -1.12 \times 10^5$ for the dielectric constant and $\sigma_{Au} = 4.01 \times 10^7$ S/m [46]. Since its results are in good agreement with measurements, the seven parameter double Debye model from [47] was used for the material simulation of water [5]. Because the modeling of a correct DNA film that is assumed to form during the functionalization procedure is exceptionally intricate, it was replaced by a 100 nm thick polymethylmethacrylate (PMMA) layer in the simulation, with $\varepsilon_{r,PMMA} = 2.6$, a dielectric loss tangent of $\delta_{PMMA} = 0.001$ and a bulk conductivity of $\sigma_{PMMA} = 1 \times 10^5$ S/m [48, 49]. The dry sensor was simulated with air, using the dielectric constant $\varepsilon_{r,air} = 1$.

2.1.2 THz spectroscopy: An all-electronic THz spectroscopy system was used in transmission mode for the dry-state measurements. The system provided a resolution of less than 6 MHz and a signal-to-noise ratio of more than 40 dB. The sensor chip was positioned employing motorized stages to accurately place the center of each query field in the focus of the THz beam. The stages have a positioning repeatability of 5 µm along all axes. The operating frequency range of 220–230 GHz results from a quasi-heterodyne detection scheme which is described in greater detail in [49, 50].

2.2 Structures and fabrication

Both sensor designs that are introduced in this work originate from a complementary Asymmetric Double Split Ring Resonator (ADSRR) unit cell design which has been described in [52]. This asymmetric design consists of two coupled resonators with different lengths, resulting in a so-called Fano resonance in the frequency response, which is particularly steep, allowing for highly sensitive measurements. The designs are used to create periodic arrays of the corresponding layout. As can be seen from Figure 2a) and d), the two designs share several properties, such as the basic ADSRR structure based on two arcs with different length, their symmetry along an axis parallel to polarization direction of the incident radiation, their composition and manufacturability by the same fabrication process. Both designs are so-called complementary metasurfaces since the resonators are slits in a metallic surface on top of a supporting substrate. These can be derived from the non-complementary design by applying Babinet's principle [53, 54]. Their general construction is composed of a quartz glass substrate (fused silica UV grade) with a thickness of 500 µm, metallized with a 10 nm chromium (Cr) layer that functions as a bonding agent for a 200 nm gold (Au) layer, followed by another 10 nm Cr layer as surface passivation. One key design objective of both layouts is the introduction of a 3 µm wide undercut etch, displayed in Figure 2b) and c). The layout in Figure 2a) has already been used in a biosensor chip and thus has been fabricated already. Details on the fabrication are described in [49]. For the layout in Figure 2d), we have completed the simulations. Its major design feature is the substrate-integrated microfluidic channel that connects the cavities formed by the resonator arcs. To close off the microfluidic system, a quartz glass cover with a thickness of 500 µm can be bonded directly to the metasurface.

2.3 Sample preparation and functionalization procedure

2.3.1 Chemicals: The 25 base pair (bp) DNA sequence based on beta-actin mRNA is 5′-HS-TGG CAC CAC ACC TTC TAC AAT GAG C-3′ (**sBA1-ssDNA**) for the capture molecules with a thiol functional group (HS-) at the 5′-end, and 5′-G CTC ATT GTA GAA GGT GTG GTG CCA-FLU-3′ (synthetic beta-actin single stranded DNA or short **sBA2-ssDNA**) for target probes. This target probe is equipped with a fluorescence marker (-FLU) at its 3′-end for further investigation purposes which

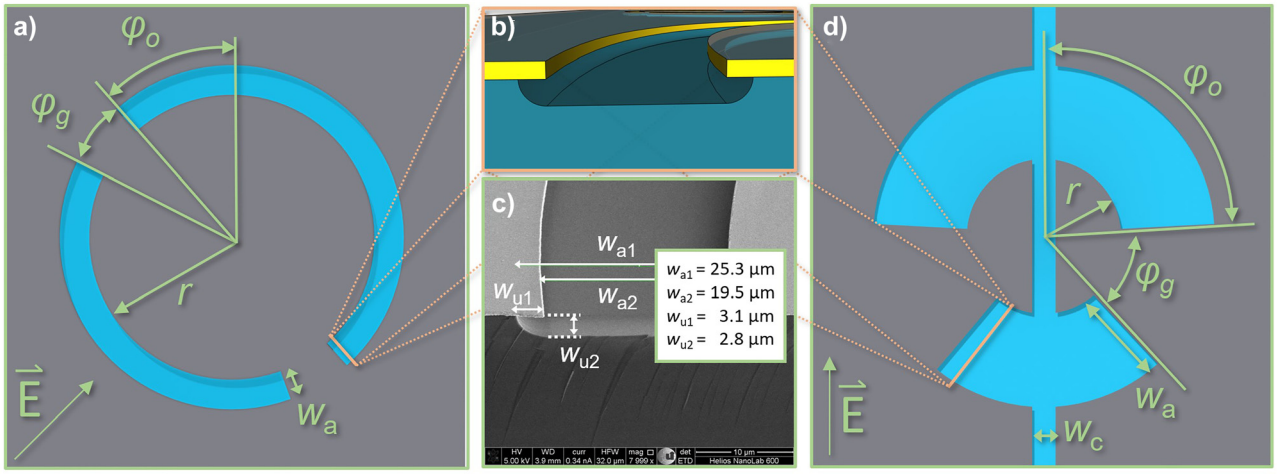

Figure 2: Resonator structures used over the course of this work. a) Schematic depiction of ADSRR for dry state measurements with a design resonance frequency f_R = 280 GHz. The gray colored areas symbolize the metallized regions, whereas the underlying fused silica substrate being exposed in the slit area is depicted in blue. The periodicity of the array is p = 416 µm, the resonator radius r = 96 µm, the arch width w_a = 20 µm, the offset angle ϕ_o = 42° and the gap angle ϕ_g = 22°. The excitation radiation propagates perpendicular to the sensor surface and is polarized in the direction indicated by $\vec{E}$. b) Schematic depiction of the undercut etch as a intersection along the indicated lines in a) and d). The fused silica substrate is displayed in blue, the gold layer in yellow. The extremely thin chromium bonding agent and protective layers are colored gray. This graphic does not depict the dimensions to scale. c) SEM picture of the undercut etch intersection with corresponding distance measurements. The etch depth w_{u2} = 2.8 µm and the width of the undercut etch w_{u1} = 3.1 µm are in good agreement with each other. d) Schematic layout of ADSRR with incorporated microfluidic channel for measurements of aqueous analyte solutions. The design resonance frequency is f_R = 250 GHz, the periodicity of the array p = 416 µm, the resonator radius r = 66 µm, the arch width w_a = 80 µm, the channel width w_c = 20 µm, the offset angle ϕ_o = 87° and the gap angle ϕ_g = 50°. The excitation radiation propagates perpendicular to the sensor surface and is polarized in the direction indicated by $\vec{E}$ [33, 51].

was not utilized in the scope of this work. In their hybridized form, these DNA oligomers are hereinafter referred to as BA double stranded DNA (**BA-dsDNA**). The 24 bp DNA sequence derived from MIA mRNA is: 5′-HS-GGT CCT ATG CCC AAG CTG GCT GAC-3′ (**sMIA1-ssDNA**) for the synthetic capture molecules carrying a thiol functional group at their 5′-end and 5′-GTC AGC CAG CTT GGG CAT AGG ACC-FLU-3′ (**sMIA2-ssDNA**) for the synthetic target probes. In their hybridized form they are hereinafter referred to as (**sMIA-dsDNA**). The thiol groups of the capture DNA sequences (**sBA1-ssDNA** and **sMIA1-ssDNA**) are protected by a mercaptohexanol (MCH) moiety forming a disulfide bond. The oligonucleotides above were synthesized by Eurofins Genomics GmbH. The molecule **rtMIA2-ssDNA** has the exact same sequence as **sMIA2-ssDNA** but does not carry the fluorescent marker FLU at its 3′-end since it is generated by reverse transcription from melanoma cells as described in chapter 2.3.4. TRIS buffer solution contains NaCl (1 mol/L), Tris-HCl (10 mmol/L), EDTA (1 mmol/L) and NaOH to adjust the pH-value to pH = 7.5. The E.Z.N.A. Total RNA Kit I (RNA Kit I) was purchased at Omega Bio-tek and the reverse transcriptase SuperScript II (reverse transcriptase Kit II) was purchased at Invitrogen AG. The reverse transcriptase reaction buffer system contains 1 µL reverse-transcriptase buffer II, 4 µL first-strand buffer (TRIS-HCl [250 mmol/L, pH = 8.3], KCl [375 mmol/L], $MgCl_2$ [15 mmol/L]), 2 µL DTT (0.1 mol/L), 1 µL dNTPs (10 µmol/L, purchased at Genaxxon bioscience GmbH), 1 µL random primer dN6 (purchased at Roche Deutschland Holding GmbH) and bidestilled water, adding up to 20 µL.

2.3.2 Sample preparation of *ex-situ* hybridized sBA-dsDNA: A solution of tris(2-carboxyethyl)phosphin (TCEP, 1 mmol/L, 10 µL) was added to a solution of capture **sBA1-ssDNA** (1 nmol) in TRIS buffer (190 µL) and stirred at room temperature for 3–4 h. A solution of **sBA2-ssDNA** (1 nmol) in TRIS buffer (200 µL) was added and stirred at 50 °C for 8 h. The resulting **sBA-dsDNA** solution was purified by centrifuging the reaction mixture in Bio-Spin P-6 Gel Columns at 1000*g* for 4 min.

2.3.3 Sensor functionalization and THz measurement with *ex-situ* hybridized sBA-DNA: Prior to any adsorption steps, each sensor was cleaned by submerging it in a solution of three parts H_2SO_4, 96%, and one part H_2O_2, 30%, at 75 °C for 2 h, rinsing it with deionized water, drying in a N_2 stream and heating it to 50 °C for 45 min. Subsequently, the resonance frequency of each query field was recorded. Several query fields (later referred to as sample fields) were covered with a solution of **sBA-dsDNA** (5 µmol/L in TRIS buffer, 3 µL each) while the nominated reference fields were kept clean. After an adsorption period of 45 min at room temperature, the sensor was rinsed with deionized water, dried in a N_2 stream and tempered at 50 °C for 45 min. The resonance frequency of each query field was recorded.

2.3.4 Preparation of rtMIA2-ssDNA and sMIA-ssDNA solutions: After cultivating the melanoma cell line Mel Im and pelleting the cells by centrifuging (approximately 3×10^6 cells per pellet), RNA Kit I was

used according to the manufacturer's instructions. The thus obtained RNA (500 ng) was dissolved in reverse transcriptase buffer solution (20 µL) and treated with reverse transcriptase Kit II according to the manufacturer's protocol at 37 °C for 45 min using dN6 primer. Ribonuclease (1 µL) was added and incubated at 37 °C for 30 min. No additional PCR amplification was performed in this study. The generated amount of **rt-ssDNA** reflects the endogenous amount of RNA in the Mel Im cells 1:1, containing a small fraction of approximately 0.000048% **rtMIA2-ssDNA**which is equal to a total target analyte amount of 4.64×10^{-18} mol. Separately, a solution of TCEP (1 mmol/L, 2 µL) was added to a solution of capture **sMIA1-ssDNA** (1 nmol) in TRIS buffer (48 µL) and stirred at room temperature for 3–4 h. In a separate vial, a solution of **sMIA2-ssDNA** (1 nmol) was prepared in TRIS buffer (50 µL).

2.3.5 Sensor functionalization and THz measurement with *on-chip* hybridized MIA-DNA: Prior to any adsorption steps, each sensor was cleaned by submerging it in a solution of three parts H_2SO_4, 96%, and one part H_2O_2, 30%, at 75 °C for 2 h, rinsing it with deionized water, drying in a N_2 stream and heating it to 50 °C for 45 min. The nominated sample fields were covered with a solution of **sMIA1-ssDNA** (20 µmol/L in TRIS buffer, 3 µL each) while the nominated reference fields were kept clean. After an adsorption period of 45 min at room temperature, the sensor was rinsed with deionized water, dried in a N_2 stream, tempered at 50 °C for 45 min and the resonance frequency of each query field was recorded. The designated sample fields were covered with a solution of MCH (1 mmol/L, 3 µL each), while the reference fields were kept clean. After an adsorption period of 45 min at room temperature, the sensor was rinsed with deionized water, dried in a N_2 stream, tempered at 50 °C for 45 min and the resonance frequency of each query field was recorded. Finally, half of the designated sample fields were covered with a solution of **sMIA2-ssDNA** (20 µmol/L in TRIS buffer, 3 µL each), while the other half was covered with the **rt-ssDNA** (**rtMIA2-ssDNA** approximately 1.55×10^{-12} mol/L, 3 µL each). The reference fields were kept clean. After a hybridization period of 45 min at room temperature, the sensor was rinsed with deionized water, dried in a N_2 stream, tempered at 50 °C for 45 min and the resonance frequency of each query field was recorded.

3 Results and discussion

3.1 Simulation results and discussion

As can be seen in Figure 3 a), the electric field concentration is highly confined at the edges of the arc-shaped slits in the metal layer. From the intersection view in Figure 3b) it becomes apparent, that this concentration is radially distributed along the free-standing edges of the arcs. However, it is slightly asymmetric and distributed towards the quartz substrate undercut etch. It is assumed that the elevated field concentration in the corner of the undercut etch originates from its rectangular shape. Due to the isotropic etch this geometry does not exist in the fabricated sensors and the simulation artefact can thus be neglected. The frequency response of the ADSRR array results in a so-called Fano-type resonance feature in the simulated transmission spectrum (cf. Figure 3c)). The characteristic properties are given in the figure description. One additional important quality of the resonance feature is the steepness of its flank which amounts to approximately −2.71 dB/GHz. The reference transmission spectrum was generated assuming only air to surround the metasurface, while the DNA transmission spectrum was

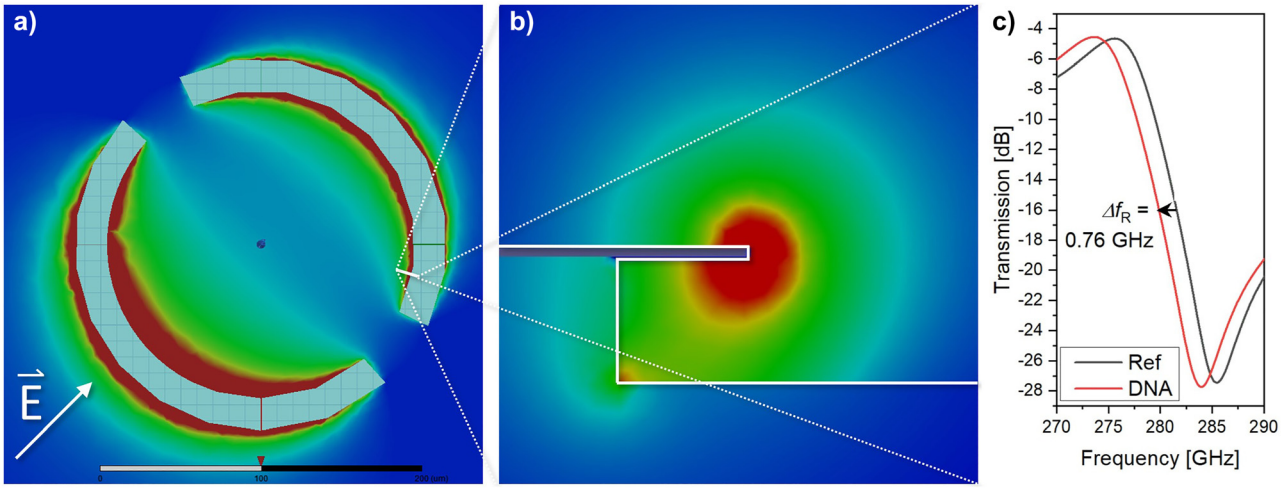

Figure 3: Dry state simulation results. a) Top view and b) intersection view of the simulated electric field distribution. The areas with the highest electric field concentration are depicted in red, while those with the lowest electric field concentration are colored ultramarine blue. The polarization direction of the THz excitation radiation is indicated by $\vec{E}$. c) Transmission spectrum for ADSRR structure from Figure 2a). The gray graph (Ref) displays the clean structure, while the red graph (DNA) results from a dielectrically loaded resonator as a DNA model system. The peak-to-peak transmission intensity difference is approximately 23 dB for both cases with a width of 8.5 GHz. At the intersection point of −16 dB the resonance frequency shift is $\Delta f_R = -0.76$ GHz [33].

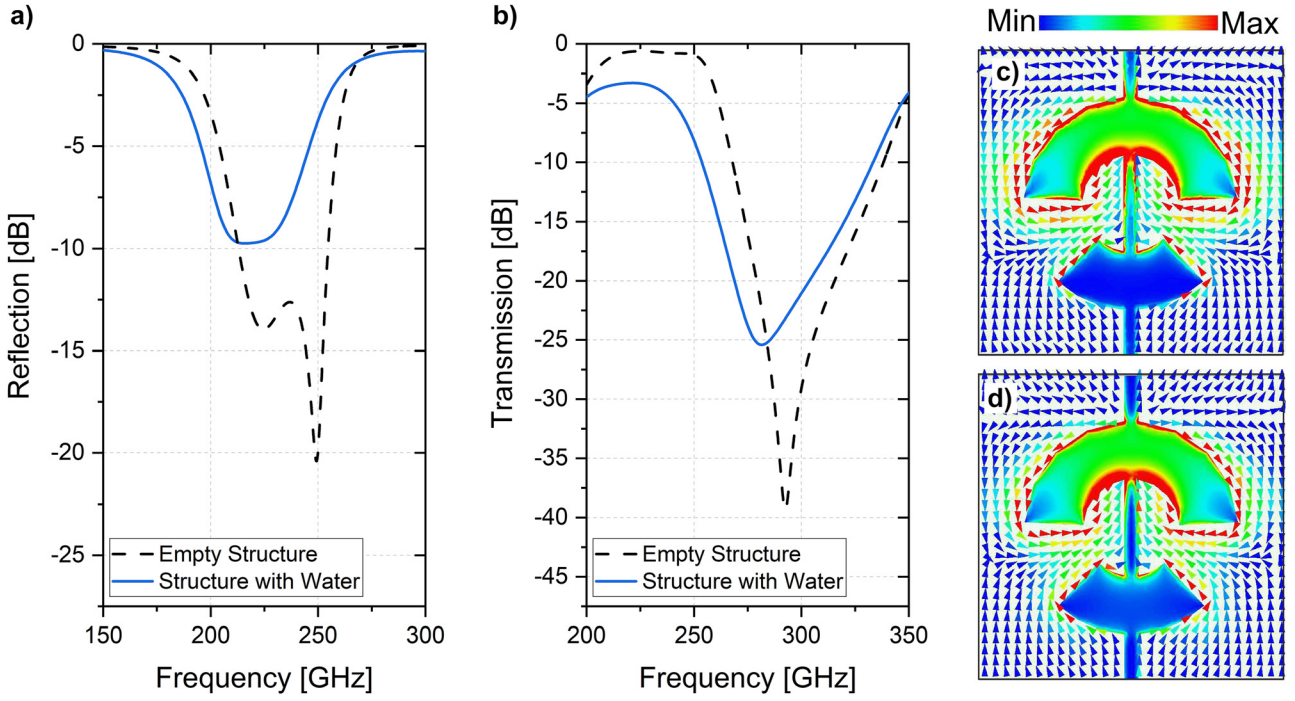

Figure 4: Simulation results for ADSRR structures from Figure 2d) for measurements in aqueous solutions. a) S11 parameter for the dry sensor (dashed line) and for the water-filled microfluidic cavity (solid line). b) S21 parameter for the dry sensor (dashed line) and the water-filled microfluidic cavity (solid line). The two right graphs are shown for the comparison of the electric field and the surface current distribution of the c) empty cavity and d) the water-filled cavity at each 230 GHz. c) And d) were reproduced from [51], with the permission of AIP Publishing.

generated using the PMMA model system, mimicking a thin layer of DNA oligomers in all the areas with exposed Au [51]. The resonance frequency of each scenario was determined by the intersection point at –16 dB and the difference of the two simulations was calculated resulting in the resonance frequency shift $\Delta f_R = -0.76$ GHz.

The simulation results for a different structure that was optimized with regard to their arc width, channel width, etch depth, offset angle and gap angle in [51] is shown in Figure 4. The reflection and transmission results are displayed for a case, when the structure is filled with air and for a case when the structure is filled with water and secluded by a quartz cover. In both scenarios, the frequency characteristic response is dominated by a Fano-type double resonance feature (DRF) in the transmission spectrum (Figure 4b)). In the air-filled scenario, the flank steepness amounts to 2.4 dB/GHz with a resonance frequency of 292.5 GHz. In the water-filled case, the slope at the flank is –0.7 dB/GHz with a resonance frequency of 281.5 GHz. The DRF can be described as dampened and shifted towards lower frequencies by the substitution of air with water. Regarding the E-field concentration and the surface current distribution it can be seen clearly from Figure 4c) and d) that there is almost no difference between the empty cavity and the water-filled cavity due to the well-chosen structural design. We assume that this comparable behavior is the reason why the Fano resonance feature is still detectable even in aqueous solutions with strong absorptions in the THz regime [51]. In order to assess the sensor performance and compare the air-filled case with the water-filled scenario, the sensitivity was determined in units of resonance frequency shift per refractive index unit (RIU), $\Delta f_R/\Delta n$ (GHz/RIU). As depicted in Figure 5, the variation of the refractive index was accomplished from $n = 1.0$ to $n = 1.9$ in the scope of this work. A more detailed analysis can be found in [51]. The resulting sensitivity for the air-filled case is 7.4 GHz/RIU, while taking water losses into account in the water-filled case, it is 6.74 GHz/RIU. All in all, the performance of both cases (the lossless air-filled scenario and the lossy water-filled scenario) remain similar to each other despite the reduced steepness of the DRF. Not only does this sensor design enable a conservation of the DRF in a microfluidic application, it does so only marginally forfeiting sensing performance and sensitivity.

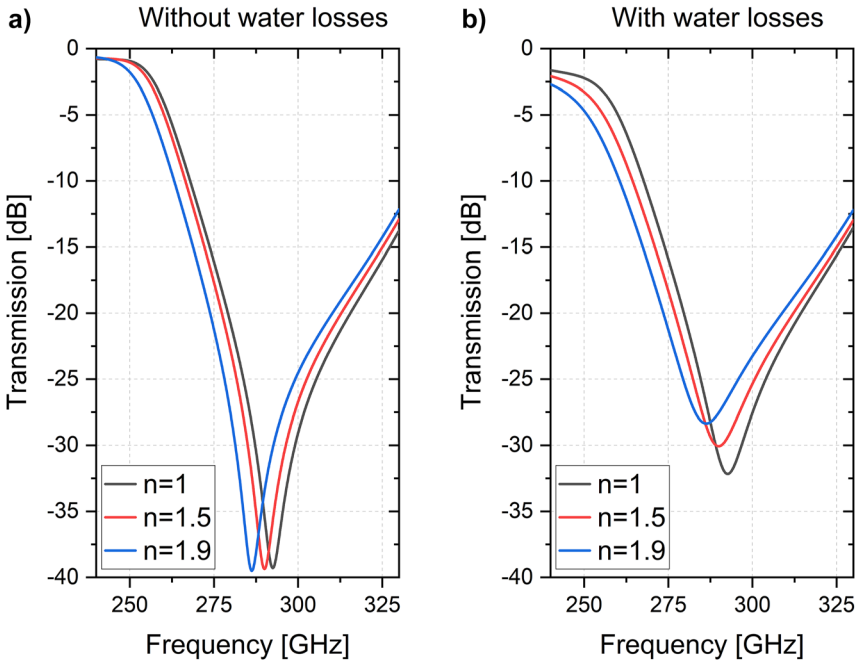

Figure 5: Amplitude transmission spectra in a) the dry state and b) the water-filled case for different refractive indices *n* [51].

3.2 Measurement results and discussion

3.2.1 Measurements with *ex-situ* hybridized sBA-dsDNA

All measurements were carried out 10 times consecutively and the standard deviation was calculated. The measurement prior to any DNA adsorption treatment is referred to as initial measurement while the measurement after the functionalization procedure is referred to as final measurement. Figure 6 shows the DRF for both the initial measurements of reference field and sample field (in the graph referred to as DNA field) and both the final measurements of reference field and DNA field. The two insets show an enlarged view on the intersection point at –15 dB, where the corresponding resonance frequencies are determined. The resonance frequency shift of the entirely untreated reference field amounts to Δf_1 = 16 ± 7 MHz towards higher frequencies, while the DNA field resonance shifts by Δf_2 = –314 ± 6 MHz to lower frequencies after the application of **sBA-dsDNA**.

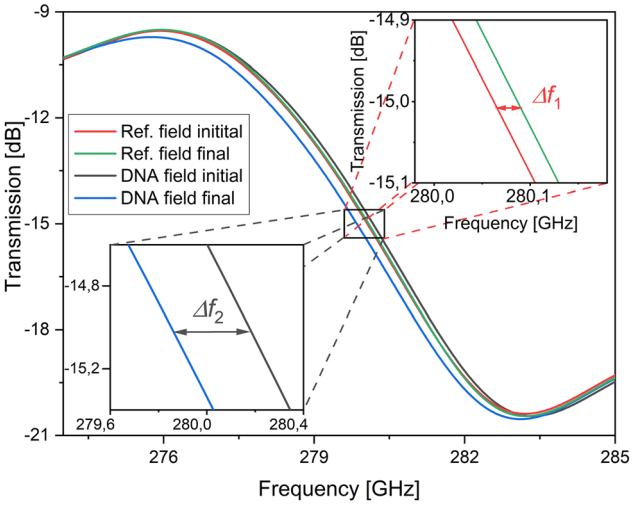

Figure 6: Exemplary transmission spectra of two query fields (reference field and DNA field) before and after the functionalization procedure. The resonance frequency f_R was determined by the intersection at –15 dB. The resonance shifts of both query fields were calculated, leading to a small shift to higher frequencies for the reference field Δf_1 = 16 ± 7 MHz, while the DNA field resonance frequency was shifted by Δf_2 = –314 ± 6 MHz to lower frequencies. The insets display the intersection area more detailed [33].

3.2.2 Measurements with *on-chip* hybridized purely synthetic and partially reverse-transcribed MIA-dsDNA

The general shape of the frequency response looks like the graphs displayed in Figure 6. In Figure 7, the resonance frequency shifts of one reference field, one sample field with purely synthetic **sMIA-DNA** and one sample field with partially synthetic and partially reverse-transcribed **rtMIA-DNA** are shown. The different functionalization steps are reflected by the colored data points. Since the graphs depict the frequency shift, the results of the initial measurement are automatically set to 0 GHz and were omitted therefore. The dark gray square represents the measurement after thiol-functionalized **sMIA1-ssDNA** was

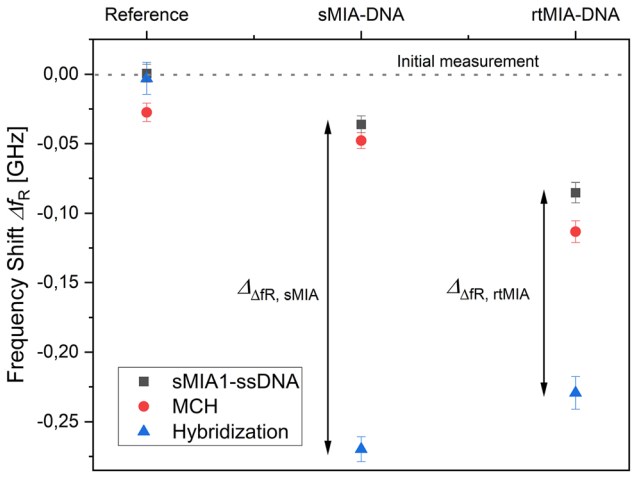

Figure 7: Relative resonance frequency shifts resulting from different surface functionalization on reference and sample query fields. The reference field is preserved unmodified throughout the entire measurement, while the sample fields sMIA-DNA and rtMIA-DNA are treated according to the functionalization steps in the legend [33].

applied to both sample fields (referred to as sMIA-DNA and rtMIA-DNA in Figure 7). The resonance frequency of the reference field does not undergo a significant shift while the sample field sMIA-DNA has a lower resonance frequency after the application of **sMIA1-ssDNA** than before. The shift in this case amounts to –36 MHz. The rtMIA-DNA field shows an even larger resonance frequency shift of –85 MHz after this step. The red circle represents the measurement after MCH treatment of the sensor. Since all query fields (including the reference field which was kept untreated) show a shift in resonance frequency of approx. –20 MHz to –25 MHz compared to the resonance frequency level from the previous step, it is reasonable to assume that this shift results from mechanical or chemical handling and can be neglected. Up to this point, the sample fields (sMIA-DNA field and rtMIA-DNA field) were treated equally. The blue upward-pointing triangle represents the measurement after the *on-chip* hybridization step with either **sMIA2-ssDNA** on the sMIA-DNA sample field, yielding a frequency shift of –270 MHz, or **rtMIA2-ssDNA** on the rtMIA-DNA sample field which results in a frequency shift of –230 MHz. The difference in resonance frequency shift between the state of applied **sMIA1-ssDNA** and the hybridized state with **sMIA2-ssDNA** $\Delta_{\Delta f,sMIA}$ is –234 MHz, compared to $\Delta_{\Delta f,rtMIA}$ = –145 MHz for the hybridization with **rtMIA2-ssDNA**.

3.2.3 Discussion of the measurement results

During the functionalization procedure, there are several chemical reactions that come into play. The first step, in which a capture DNA single strand is applied to the sensor surface, relies on the strong chemical bond between Sulfur (S) and Gold (Au). The different capture strands are all equipped with a so-called thiol functional group at the 5′-end that consists of a sulfur atom and a hydrogen atom. The hydrogen atom is cleaved off over the course of the S-Au bond formation. Since this S-Au bond is comparatively strong, molecules containing thiol groups carry the ability to form self-assembled monolayers (SAM) on gold interfaces [55, 56]. Due to the clever design of both introduced biosensor layouts, the areas with exposed gold match with the regions of high electric field concentration, thereby increasing the nominal sensitivity towards molecules with thiol functionality. It can be seen from Figure 6 that the biosensor experienced a change in refractive index for the field that was exposed to the **sBA-dsDNA** solution previously. It can be concluded that the thiol-carrying dsDNA most likely adsorbed to the baer Au areas of the sensor, thereby causing the shift in resonance frequency. The same behavior can be observed in Figure 7 looking at the **sMIA1-ssDNA** treatment that caused a shift in resonance frequency to lower frequencies, as well. Due to the different refractive indices of ssDNA and dsDNA, the two results are comparable only restrictedly in qualitative manner. Under standard conditions, DNA molecules tend to unselectively losely adsorb onto an exposed Au surface, too. Resulting from their elongated shape, they can do so even when their “sulfur anchor” has bound to the gold. Those molecules, however are not readily available for further binding events such as hybridization. In order to remove these losely adsorbed molecules or force them into a position in which they are available for further functionalization treatments, they can be displaced by another thiol-carrying molecule. By choosing a low molecular weight compound with certain chemical polarity properties such as MCH for this task, this process can be completed quite efficiently and has become a standard measure for this purpose [55, 56]. An additional advantage of this step is that it prevents later unselective binding by effectively shielding the Au-surface. The SAM of MCH does not significantly affect the dielectric environment of the ADSRR as can be deduced from the extremely small difference in resonance frequency after the MCH

treatment. Given, that the difference between gray square and respective red circle data points in Figure 7 is almost identical to the one of the reference field which was not exposed to MCH solution, it can be assumed that the observed small resonance frequency shift originates from a general mechanical or chemical handling issue. The precise sequence of DNA molecules is one of their most essential properties. It is also responsible for their extremely high specificity. In a simplified model, a single DNA strand will only bind to its complementary strand and – depending on its length – does not even tolerate minor deviations in sequence. This process, if successful, is called hybridization. In the context of biosensing, this selective binding behavior can be exploited for the purpose of highly selective analyte detection. In our example, the large shift in resonance frequency between the blue triangular data points and the red circular data points in Figure 7 allows the deduction, that the target DNA molecules and the ones that had been immobilized on the sensor surface before were hybridized and can thus be called complementary to each other. The rinsing step during biosensor preparation would have removed all unselectively adsorbed molecules. One interesting observation that can be made by comparing these hybridization-based resonance shifts with each other is that their magnitude is quite similar despite the large difference in concentration and correspondingly in amount of substance. The synthetic complementary **sMIA2-ssDNA** solution had a concentration of 20 µmol/L while the concentration of **rtMIA2-ssDNA** in the **rt-ssDNA** solution amounted to only 1.55×10^{-12} mol/L approximately. Still, the shift caused by the reverse-transcribed target DNA reached 62% of the shift caused by the highly concentrated synthetic sample. This can be explained by the fact that the area with exposed gold, where the capture-DNA molecules can be immobilized, is limited. Also, these molecules only attain a certain surface density. The number of hybridization partners is therefore restricted, too. The results displayed in Figure 7 ultimately suggest that the number of hybridization partners was occupied to 62% by the number of target molecules in the applied 3 µL volume of **rt-ssDNA** solution.

4 Conclusions

We have shown a detailed overview of our recent research in the field of THz biosensing with significant achievements in high-sensitivity and highly specific analysis of tumor marker RNA at physiological concentrations as well as significant development towards THz biosensing in aqueous environments. Our THz biosensor for DNA detection in the dry state is carefully designed to achieve exceptionally high sensitivity and specificity using complementary ADSRR structures with undercut etch. Our biosensor features high field concentration combined with a localized biochemical sensor modification at the positions with highest field concentration. Thereby, the interaction of the THz radiation with the analyte is further enhanced, and at the same time the necessary analyte volume is reduced. The biochemical sensor modification ensures high specificity of the analysis by utilizing capture molecules with thiol functionality bound to the gold surface. The careful sensor design allowed for the label-free THz detection of the tumor-marking mRNA sequence MIA in concentrations as low as 1.55×10^{-12} mol/L without the need for biochemical amplification and labeling during sample preparation. This remarkable achievement clearly demonstrates the high potential for THz biosensing not only limited to detection of single biomolecules, but also expandable towards analysis of different analytes in one biological sample.

Based on this elementary sensor layout, we have created and analyzed one particular design for THz measurements in aqueous environment by detailed electromagnetic simulations with parameter variations. An optimized sensor design with substrate-integrated microfluidics is proposed, that maintains its resonance feature even for the water-filled case. The interaction volume of THz radiation and water is kept at a minimum by the design of the microfluidic channels. The clever design allows for relatively easy manufacturing, since the etching and substrate-integrated microfluidic channels are fabricated using the same mask without the necessity of an additional alignment and fabrication step. Our simulations show, that the electric field concentration in the single sensor elements stays almost the same, while the resonance feature in the frequency response is slightly dampened and shifted towards lower frequencies for the water-filled case. This demonstrates, that the substrate-integrated microfluidics only marginally influence the electromagnetic properties of our sensor design for measurements in highly absorbing liquids. These results provide a significant and very promising step towards THz measurements of biological systems in their natural environment.

Acknowledgement: We thank the University of Siegen for providing the OMNI cluster for high performance computing. Moreover, we thank Micronit GmbH for the implementation of a successful sensor fabrication process.

We thank the MNaF center of instruments, namely Petra auf dem Brinke and Thorsten Staedler for assisance with SEM imaging.

Author contributions: All the authors have accepted responsibility for the entire content of this submitted manuscript and approved submission.

Research funding: This work is part of the national priority program SPP 1857 ESSENCE which was funded by the Deutsche Forschungsgemeinschaft (DFG, German Research Foundation) under the contract numbers BO 1573/27, HA 3022/8 and WI 5209/1.

Conflict of interest statement: The authors declare no conflicts of interest regarding this article.

References

[1] I. Amenabar, F. Lopez, and A. Mendikute, "In introductory review to THz non-destructive testing of composite matter," *J. Infrared, Millim. Terahertz Waves*, vol. 34, pp. 152–169, 2013.

[2] P. U. Jepsen, D. G. Cooke, and M. Koch, "Terahertz spectroscopy and imaging – modern techniques and applications," *Laser Photon. Rev.*, vol. 5, no. 1, pp. 124–166, 2011.

[3] D. M. Mittleman, R. H. Jacobsen, and M. C. Nuss, "T-ray imaging," *IEEE J. Sel. Top. Quant. Electron.*, vol. 2, pp. 679–692, 1996.

[4] R. M. Smith and M. A. Arnold, "Terahertz time-domain spectroscopy of solid samples: principles, applications, and challenges," *Appl. Spectrosc. Rev.*, vol. 46, no. 8, pp. 636–679, 2011.

[5] C. Weisenstein, A. K. Wigger, M. Richter, R. Sczech, A. K. Bosserhoff, and P. Haring Bolívar, "THz detection of biomolecules in aqueous environments—status and perspectives for analysis under physiological conditions and clinical use," *J. Infrared, Millim. Terahertz Waves*, vol. 42, no. 6, pp. 607–646, 2021.

[6] B. Ferguson and X.-C. Zhang, "Materials for terahertz science and technology," *Nat. Mater.*, vol. 1, no. 1, p. 26, 2002.

[7] B. Fischer, S. Wietzke, M. Reuter, et al., "Investigating material characteristics and morphology of polymers using terahertz technologies," *IEEE Trans. Terahertz Sci. Technol.*, vol. 3, no. 3, pp. 259–268, 2013.

[8] M. Tonouchi, "Cutting-edge terahertz technology," *Nat. Photonics*, vol. 1, no. 2, pp. 97–105, 2007.

[9] P. Siegel, "Terahertz technology," *IEEE Trans. Microw. Theor. Tech.*, vol. 50, no. 3, pp. 910–928, 2002.

[10] Z. Taylor, R. Singh, D. Bennett, et al., "THz medical imaging: in vivo hydration sensing," *IEEE Trans. Terahertz Sci. Technol.*, vol. 1, no. 1, pp. 201–219, 2011.

[11] X. C. Zhang, "Terahertz wave imaging: horizons and hurdles," *Phys. Med. Biol.*, vol. 47, p. 3667, 2002.

[12] A. D. Weston and L. Hood, "Systems biology, proteomics, and the future of health care: toward predictive, preventative, and personalized medicine," *J. Proteome Res.*, vol. 3, no. 2, pp. 179–196, 2004.

[13] X. Fan, I. M. White, S. I. Shopova, H. Zhu, J. D. Suter, and Y. Sun, "Sensitive optical biosensors for unlabeled targets: a review," *Anal. Chim. Acta*, vol. 620, nos. 1–2, pp. 8–26, 2008.

[14] H. Hansma, K. Kim, D. Laney, et al., "Properties of biomolecules measured from atomic force microscope images: a review," *J. Struct. Biol.*, vol. 119, no. 2, pp. 99–108, 1997.

[15] W. F. Patton, "Detection technologies in proteome analysis," *J. Chromatogr. B*, vol. 771, nos. 1–2, pp. 3–31, 2002.

[16] A. Malon, T. Vigassy, E. Bakker, and E. Pretsch, "Potentiometry at trace levels in confined samples: ion-selective electrodes with subfemtomole detection limits," *J. Am. Chem. Soc.*, vol. 128, no. 25, pp. 8154–8155, 2006.

[17] G. Madelin, R. Kline, R. Walvick, and R. R. Regatte, "A method for estimating intracellular sodium concentration and extracellular volume fraction in brain in vivo using sodium magnetic resonance imaging," *Sci. Rep.*, vol. 4, p. 4763, 2014.

[18] J. Xu, K. W. Plaxco, S. J. Allen, J. E. Bjarnason, and E. R. Brown, "0.15–3.72 THz absorption of aqueous salts and saline solutions," *Appl. Phys. Lett.*, vol. 90, no. 3, p. 031908, 2007.

[19] D. A. Schmidt, O. Birer, S. Funkner, et al., "Rattling in the cage: ions as probes of sub-picosecond water network dynamics," *J. Am. Chem. Soc.*, vol. 131, no. 51, pp. 18512–18517, 2009.

[20] W. Qiao, K. Yang, A. Thoma, and T. Dekorsy, "Dielectric relaxation of HCl and NaCl solutions investigated by terahertz time-domain spectroscopy," *J. Infrared, Millim. Terahertz Waves*, vol. 33, no. 10, pp. 1029–1038, 2012.

[21] Sigma-Aldrich, "Mak181 – high sensitivity glucose assay kit," 2019. Available at: https://www.sigmaaldrich.com/DE/de/product/sigma/mak181.

[22] K. Serita, H. Murakami, I. Kawayama, and M. Tonouchi, "A terahertz-microfluidic chip with a few arrays of asymmetric meta-atoms for the ultra-trace sensing of solutions," *Photonics*, vol. 6, no. 1, p. 12, 2019.

[23] A. M. Gressner and T. Arndt, *Lexikon der Medizinischen Laboratoriumsdiagnostik*, Berlin, Heidelberg, Springer Berlin Heidelberg, 2013.

[24] Enzo Life Sciences, Inc., "Camp complete elisa kit (2019)," 2019. Available at: https://www.enzolifesciences.com/ADI-900-163A/camp-complete-elisa-kit/.

[25] P. Glancy and W. P. Beyermann, "Dielectric properties of fully hydrated nucleotides in the terahertz frequency range," *J. Chem. Phys.*, vol. 132, no. 24, p. 245102, 2010.

[26] V. Ip, M. J. McKeage, P. Thompson, D. Damianovich, M. Findlay, and J. J. Liu, "Platinum-specific detection and quantification of oxaliplatin and pt(r, r-diaminocyclohexane)cl2 in the blood plasma of colorectal cancer patients," *J. Anal. Atomic Spectrom.*, vol. 23, no. 6, p. 881, 2008.

[27] X. Wu, Y. E, X. Xu, and L. Wang, "Label-free monitoring of interaction between DNA and oxaliplatin in aqueous solution by terahertz spectroscopy," *Appl. Phys. Lett.*, vol. 101, no. 3, p. 033704, 2012.

[28] Company Abcam plc, "Albumin human elisa kit (ab179887) (2019)," 2019. Available at: https://www.abcam.com/human-albumin-elisa-kit-ab179887.html.

[29] R. Zhang, Q. Chen, K. Liu, et al., "Terahertz microfluidic metamaterial biosensor for sensitive detection of small-volume liquid samples," *IEEE Trans. Terahertz Sci. Technol.*, vol. 9, no. 2, pp. 209–214, 2019.

[30] Y. Sun, Y. Zhang, and E. Pickwell-Macpherson, "Investigating antibody interactions with a polar liquid using terahertz pulsed spectroscopy," *Biophys. J.*, vol. 100, no. 1, pp. 225–231, 2011.

[31] Company Abcam plc, "Albumin human elisa kit (ab195215) (2019)," 2019. Available at: https://www.abcam.com/human-igg-elisa-kit-ab195215.html.
[32] U. Schauer, F. Stemberg, C. H. L. Rieger et al., "Igg subclass concentrations in certified reference material 470 and reference values for children and adults determined with the binding site reagents," *Clin. Chem.*, vol. 49, no. 11, pp. 1924–1929, 2003.
[33] C. Weisenstein, D. Schaar, A. Katharina Wigger, H. Schäfer-Eberwein, A. K. Bosserhoff, and P. Haring Bolívar, "Ultrasensitive THz biosensor for PCR-free cDNA detection based on frequency selective surfaces," *Biomed. Opt Express*, vol. 11, no. 1, pp. 448–460, 2020.
[34] T. Arikawa, M. Nagai, and K. Tanaka, "Characterizing hydration state in solution using terahertz time-domain attenuated total reflection spectroscopy," *Chem. Phys. Lett.*, vol. 457, nos. 1–3, pp. 12–17, 2008.
[35] S. A. Yoon, S. H. Cha, S. W. Jun, et al., "Identifying different types of microorganisms with terahertz spectroscopy," *Biomed. Opt Express*, vol. 11, no. 1, p. 406, 2020.
[36] M. Tang, M. Zhang, S. Yan, et al., "Detection of DNA oligonucleotides with base mutations by terahertz spectroscopy and microstructures," *PLoS One*, vol. 13, no. 1, p. e0191515, 2018.
[37] X. Chen and W. Fan, "Toroidal metasurfaces integrated with microfluidic for terahertz refractive index sensing," *J. Phys. Appl. Phys.*, vol. 52, no. 48, p. 485104, 2019.
[38] S. J. Park, S. A. Yoon, and Y. H. Ahn, "Dielectric constant measurements of thin films and liquids using terahertz metamaterials," *RSC Adv.*, vol. 6, no. 73, pp. 69381–69386, 2016.
[39] M. Chen, L. Singh, N. Xu, R. Singh, W. Zhang, and L. Xie, "Terahertz sensing of highly absorptive water-methanol mixtures with multiple resonances in metamaterials," *Opt Express*, vol. 25, no. 13, pp. 14089–14097, 2017.
[40] K. Shih, P. Pitchappa, M. Manjappa, C. P. Ho, R. Singh, and C. Lee, "Microfluidic metamaterial sensor: selective trapping and remote sensing of microparticles," *J. Appl. Phys.*, vol. 121, no. 2, p. 023102, 2017.
[41] F. Miyamaru, K. Hattori, K. Shiraga et al., "Highly sensitive terahertz sensing of glycerol-water mixtures with metamaterials," *J. Infrared, Millim. Terahertz Waves*, vol. 35, no. 2, pp. 198–207, 2014.
[42] Y. Sun, X. Xia, H. Feng, H. Yang, C. Gu, and L. Wang, "Modulated terahertz responses of split ring resonators by nanometer thick liquid layers," *Appl. Phys. Lett.*, vol. 92, no. 22, p. 221101, 2008.
[43] K. Shih, P. Pitchappa, L. Jin, C.-H. Chen, R. Singh, and C. Lee, "Nanofluidic terahertz metasensor for sensing in aqueous environment," *Appl. Phys. Lett.*, vol. 113, no. 7, p. 071105, 2018.
[44] M. Naftaly and R. E. Miles, "Terahertz time-domain spectroscopy for material characterization," *Proc. IEEE*, vol. 95, no. 8, pp. 1658–1665, 2007.
[45] D. Grischkowsky, S. Keiding, M. van Exter, and C. Fattinger, "Far-infrared time-domain spectroscopy with terahertz beams of dielectrics and semiconductors," *JOSA B*, vol. 7, no. 10, pp. 2006–2015, 1990.
[46] P. B. Johnson and R. W. Christy, "Optical constants of the noble metals," *Phys. Rev. B*, vol. 6, no. 12, pp. 4370–4379, 1972.
[47] H. J. Liebe, G. A. Hufford, and T. Manabe, "A model for the complex permittivity of water at frequencies below 1 THz," *Int. J. Infrared Millimet. Waves*, vol. 12, no. 7, pp. 659–675, 1991.
[48] Y.-S. Jin, G.-J. Kim, and S.-G. Jeon, "Terahertz dielectric properties of polymers," *J. Kor. Phys. Soc.*, vol. 49, no. 2, pp. 513–517, 2006.
[49] C. Weisenstein, D. Schaar, M. Schmeck, A. K. Wigger, A. K. Bosserhoff, and P. Haring Bolívar, "Detection of human tumor markers with THz metamaterials," in *2018 43rd International Conference on Infrared, Millimeter, and Terahertz Waves (IRMMW-THz)*, 2018, pp. 1–2.
[50] C. Debus, G. Spickermann, M. Nagel, and P. H. Bolívar, "All-electronic terahertz spectrometer for biosensing," *Microw. Opt. Technol. Lett.*, vol. 53, no. 12, pp. 2899–2902, 2011.
[51] C. Weisenstein, M. Richter, A. K. Wigger, A. Bosserhoff, and P. Haring Bolívar, "Substrate-integrated microfluidics for sensitive biosensing with complementary thz metamaterials in water," *Appl. Phys. Lett.*, vol. 120, no. 5, p. 053702, 2022.
[52] C. Debus and P. H. Bolívar, "Frequency selective surfaces for high sensitivity terahertz sensing," *Appl. Phys. Lett.*, vol. 91, no. 18, p. 184102, 2007.
[53] F. Falcone, T. Lopetegi, M. A. Laso, et al., "Babinet principle applied to the design of metasurfaces and metamaterials," *Phys. Rev. Lett.*, vol. 93, no. 19, p. 197401, 2004.
[54] C. Debus and P. H. Bolívar, "Terahertz biosensors based on double split ring arrays," in *Photonics Europe*, 2008, p. 69870U.
[55] T. M. Herne and M. J. Tarlov, "Characterization of DNA probes immobilized on gold surfaces," *J. Am. Chem. Soc.*, vol. 119, no. 38, pp. 8916–8920, 1997.
[56] R. Georgiadis, K. P. Peterlinz, and A. W. Peterson, "Quantitative measurements and modeling of kinetics in nucleic acid monolayer films using SPR spectroscopy," *J. Am. Chem. Soc.*, vol. 122, no. 13, pp. 3166–3173, 2000.